NANO LETTERS
Letter
pubs.acs.org/NanoLett

Directed Assembly of Nanoparticle Catalysts on Nanowire Photoelectrodes for Photoelectrochemical CO_2 Reduction

Qiao Kong,[†] Dohyung Kim,[‡] Chong Liu,[†,§] Yi Yu,[†] Yude Su,[†] Yifan Li,[†] and Peidong Yang[*,†,‡,§,∥]

[†]Department of Chemistry, University of California, Berkeley, California 94720, United States
[‡]Department of Materials Science and Engineering, University of California, Berkeley, California 94720, United States
[§]Materials Sciences Division, Lawrence Berkeley National Laboratory, Berkeley, California 94720, United States
[∥]Kavli Energy Nanosciences Institute, Berkeley, California 94720, United States

Supporting Information

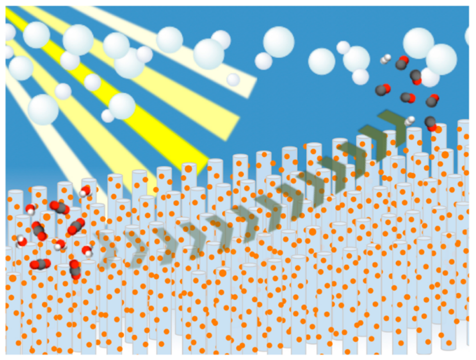

ABSTRACT: Reducing carbon dioxide with a multicomponent artificial photosynthetic system, closely mimicking nature, represents a promising approach for energy storage. Previous works have focused on exploiting light-harvesting semiconductor nanowires (NW) for photoelectrochemical water splitting. With the newly developed CO_2 reduction nanoparticle (NP) catalysts, direct interfacing of these nanocatalysts with NW light absorbers for photoelectrochemical reduction of CO_2 becomes feasible. Here, we demonstrate a directed assembly of NP catalysts on vertical NW substrates for CO_2-to-CO conversion under illumination. Guided by the one-dimensional geometry, well-dispersed assembly of Au_3Cu NPs on the surface of Si NW arrays was achieved with facile coverage tunability. Such Au_3Cu NP decorated Si NW arrays can readily serve as effective CO_2 reduction photoelectrodes, exhibiting high CO_2-to-CO selectivity close to 80% at −0.20 V vs RHE with suppressed hydrogen evolution. A reduction of 120 mV overpotential compared to the planar (PL) counterpart was observed resulting from the optimized spatial arrangement of NP catalysts on the high surface area NW arrays. In addition, this system showed consistent photoelectrochemical CO_2 reduction capability up to 18 h. This simple photoelectrode assembly process will lead to further progress in artificial photosynthesis, by allowing the combination of developments in each subfield to create an efficient light-driven system generating carbon-based fuels.

KEYWORDS: *nanowires, nanoparticle catalyst, nanoparticle assembly, artificial photosynthesis, carbon dioxide reduction*

Artificial photosynthesis is a promising energy storage method that converts solar energy to energy stored in chemical bonds.[1−8] As the name suggests, it mimics nature's energy cycle and shares some common features of complexity regarding the multiple processes involved. Photosynthesis, in general, consists of the light harvesting part, where the absorbed photons are converted to charge carriers, and the catalytic conversion part, where the charge carriers are subsequently used to drive targeted reactions. In order to assemble an efficient photosynthetic system, the utmost performance of the individual components is required as well as the optimized spatial arrangement between the components. Previous research has mainly focused on advancing solar water splitting reactions, in which efficient semiconductor light absorbers and hydrogen evolving catalysts have been combined.[9−16] Recently, a few studies have been reported for photoelectrochemical CO_2 reduction by integrating catalytic components using various methods including photoelectrode-position, atomic layer deposition, and so forth.[3,7,8,17,18] With the latest advances in discovering efficient CO_2 reducing NP electrocatalysts that have the potential to be light-driven,[19−21] it is necessary to develop an effective process for integrating these nanocatalysts with well-studied light absorbers.

Directed assembly of NP catalysts on NW light absorbers is demonstrated here to create an integrated photoelectrode for photoelectrochemical reduction of CO_2. TiO_2-protected n^+p-Si NW arrays were fabricated (Figure S1), in parallel with a Au_3Cu NP catalyst (Figure S2) featuring high turnover and mass activity for CO_2-to-CO conversion reported previously from our lab,[20] as CO is one of the attractive targets in artificial photosynthesis.[22] Photoelectrochemical production of CO in aqueous environments is appealing as it enables generation of syngas using a renewable energy source.[23,24] Syngas produced in this manner can serve as a basis for a variety of commodity chemicals converted at the downstream.[25]

In a simple drop-casting process, the NW geometry allows the NP solutions to dry in a unidirectional manner with a receding meniscus along the wires, and as a result the NPs are being uniformly decorated onto the NW surface (Figure 1a, b).

Received: June 7, 2016
Revised: July 27, 2016

DOI: 10.1021/acs.nanolett.6b02321

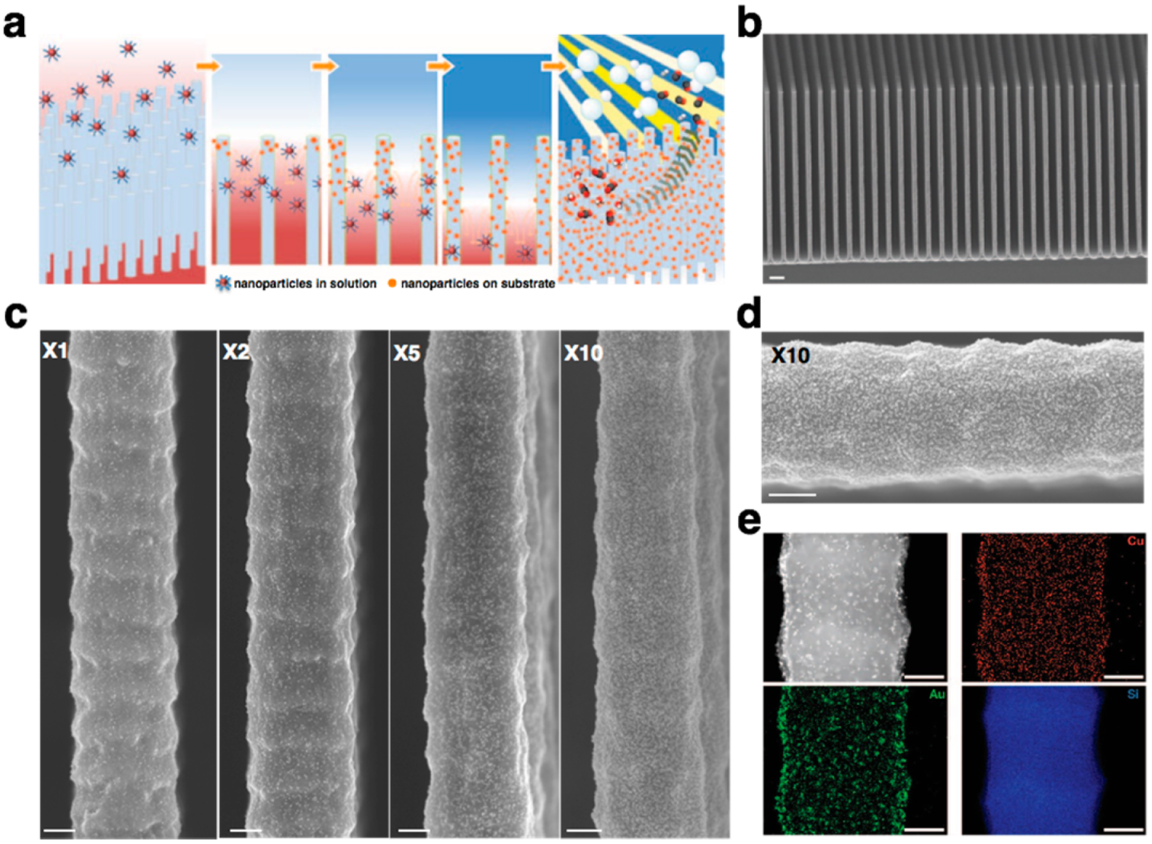

Figure 1. Au_3Cu NP assembly on Si NW arrays. (a) Schematic of the nanoparticle assembly process and the use of the integrated system for light-driven CO_2 reduction. (b) SEM image (scale bar 2 μm) of Au_3Cu NP assembled Si NW arrays. (c) SEM images (scale bar 200 nm) demonstrating uniform and tunable NP assembly on Si NW arrays. Numbers indicate loading amounts that have been proportionally varied. (d) Zoom-in image (scale bar 200 nm) of a Si NW with ×10 loading of Au_3Cu NPs uniformly assembled. (e) STEM image and elemental mapping of Au (green), Cu (red), and Si (blue). Though the thick diameter of the Si NW suppresses the contrast of Au and Cu signals to background, we can clearly see the signals originating from the NPs at the edge of the NW. Scale bars are 200 nm.

This feature is in stark contrast to what is typically observed on planar substrates, where the entire NP solution breaks up into individual droplets to form ring patterns or islands upon drying.[26] Our observation showed that the one-dimensionality of NWs served as a guide in directing the uniform spatial arrangement of NP catalysts onto the NW surface, enabling easy and reproducible assembly of the CO_2 reduction photoelectrode with well-defined semiconductor-catalyst interface.

Scanning electron microscopy (SEM) images confirm the controllable uniform assembly of individual NPs with varying loading amounts (Figure 1c). The uniformity can be maintained even for very large surface coverage (Figure 1d). This is particularly important as it allows effective utilization of their nanoscale surface for catalysis. Scanning transmission electron microscopy (STEM) and elemental mapping (Figure 1e) further confirm the presence of uniformly distributed Au_3Cu NPs. In contrast, NP assembly on planar substrates with identical procedures typically resulted in the formation of islands where nanoparticles were aggregated (Figure S3).

Quantitative analysis of NP coverage on NW arrays indeed shows a close match between experimental value and the theoretical estimate assuming NPs are well-dispersed across the NW surface (Figure 2a). The detailed analysis of different segments along the NW reveals that the NP distribution exhibits a relatively higher coverage at the top (Figure 2b and Figure S4), which could be explained by the unidirectional drying process of the NP solution guided by the NW geometry where the top section of the wires would have been exposed to a relative higher concentration of NPs (Figure 1a and Figure S5).[27,28] Our hypothesis of particle deposition with a receding meniscus along the NW surface suggests that the aspect ratio of the nanowires needs to be large enough to accommodate all the NPs in solution before the liquid front reaches the bottom part of the wires. With lower aspect ratio NWs, nearly half of the NPs settled to the base of the substrate (Figure 2c and Figure S6). This observation indicates that high surface area (relative to the NPs to be deposited) of the NWs alone is not the determining factor to guarantee a well-dispersed loading. Directed assembly process mediated by NW one-dimensionality with a sufficient aspect ratio is what allows this simple drop-casting method to be useful.

NPs being deposited onto the NWs while the liquid front moving implies an attractive interaction between the substrate surface (stationary phase) and the metal nanoparticles.[29] At the same time, a counteracting particle−solvent interaction should be present allowing NPs to stay in the solution (mobile phase). While the solution drying process is mediated by the NW substrate, a balance between these interactions at the microscopic level may also be critical.[30] To test this hypothesis, amount of surface ligands was tuned where less ligand would allow stronger interactions between the NP and the NW and vice versa. When the NPs were deprived of the ligands, identical loading procedure resulted in clustering and dense coverage at

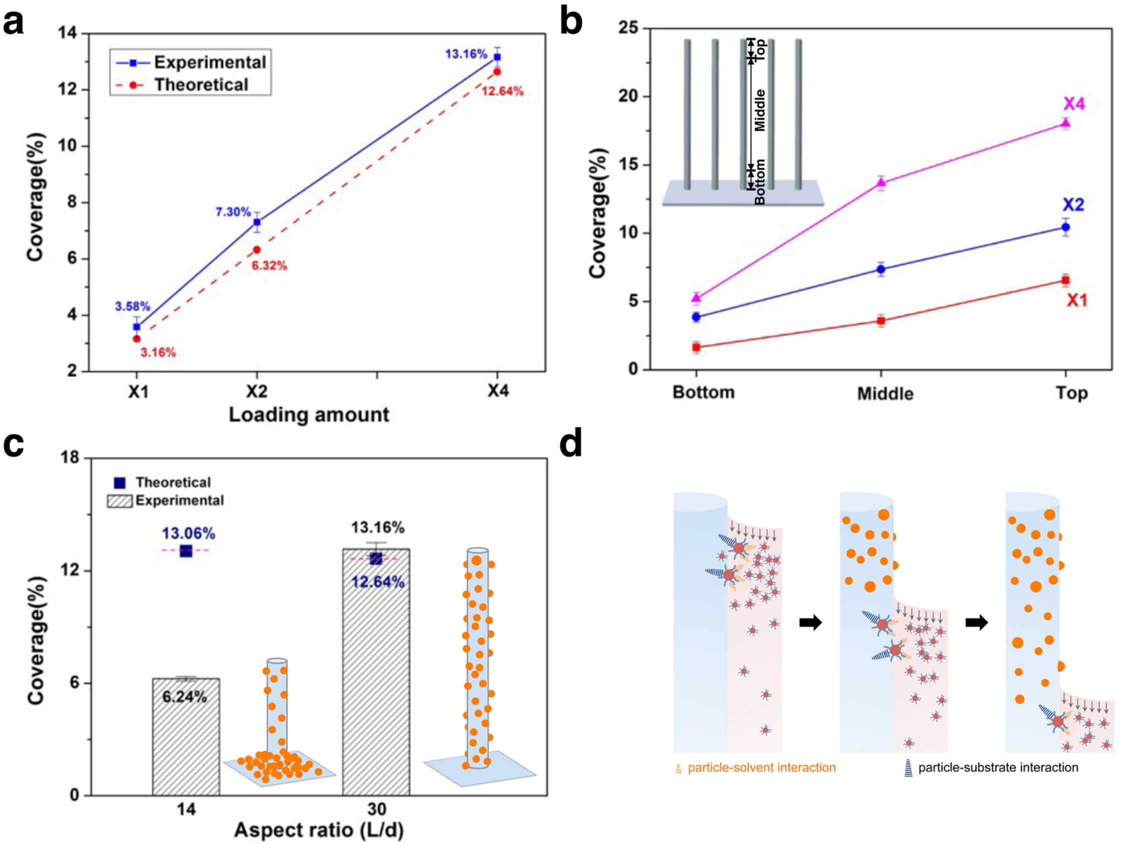

Figure 2. Quantitative analysis of NP assembly on NWs. Quantitative analysis of Au_3Cu NP assembly on (a,b) NW substrates with ×1, ×2 and ×4 loading amounts (see Methods). Experimental determination of NP coverage (area fraction out of the total area provided) on NW surface is compared to the theoretical estimate assuming NPs are isolated and well-dispersed. The numbers in (a) illustrate the overall coverage of Au_3Cu NPs on NW surface. Experimentally determined coverage is an average of multiple wires with each wire measured along its entire length. For (b), NP assembly was quantitatively analyzed by dividing each nanowire into multiple sections along its length. When divided into eight segments, six segments in the middle had NP coverages that are similar in value with a narrow deviation. The quantitative coverages of the middle section shown in (b) are an average of middle six segments on multiple wires. Top and bottom are the other two 1/8's at the end of each nanowire. (c) Effect of NW aspect ratio on NP assembly. Aspect ratio is defined as the ratio of the NW length (L) to the diameter (d). In this case, length is the only variable while the diameter is kept the same. Error bars are from quantitative analysis of multiple wires throughout each substrate. (d) Schematic of directed NP assembly under NW geometry-guided solution drying and balanced interactions.

the top part of the wires with only few NPs from the middle to the bottom segment (Figure S7). In contrast, if more ligands were introduced, a large portion of the particles was found at the base of the substrate (Figure S7). These results indicate that with the balanced interactions present, one-dimensionality of the NW geometry facilitates the directed NP assembly by simply drop-casting a NP solution and letting it dry spontaneously (Figure 2d).

Light-driven CO_2 reduction on NP decorated PL and NW substrates was performed under 20 mW/cm^2 of 740 nm illumination to take into account CO_2 mass-transport limitations in CO_2-saturated 0.1 M $KHCO_3$ under standard conditions (Figure 3a).[31] Under dark, both electrodes showed negligible current output. In contrast, greatly enhanced photocurrents were observed under illumination with both photoelectrodes exhibiting similar open-circuit voltage at around 0.25 V vs RHE, implying comparable photovoltage output. However, compared to the planar counterpart, NW substrate exhibited higher total current, which could be an indication of enhanced photoelectrochemical CO_2 reduction with lowered overpotentials (~130 mV difference at 1 mA/cm^2 compared with the planar counterpart). Detailed investigation of steady-state current densities (blue and red square symbols in Figure 3a for planar and NW photoelectrodes, respectively) also shows improved photocurrents of NW photoelectrodes (Figure S8) compared to the planar counterpart.

As CO_2 reduction typically leads to various different products, the rate of individual product formation needs to be quantified to evaluate performance. Examination through gas chromatography and quantitative nuclear magnetic resonance spectroscopy on both types of photoelectrodes reveals CO as a major product (Figure S9). H_2 and a small amount of formate (Figure S10) are detected as well. As shown in Figure 3a, NW photocathode exhibited faradaic efficiency (FE) of CO reaching close to 80% at only −0.20 V vs RHE (90 mV from the equilibrium potential for CO_2/CO), indicating 80% of the photogenerated charge extracted was used to selectively drive CO_2-to-CO conversion at the catalyst end.[20] We also observed the FE reaching a peak and declining at moderate overpotentials, likely due to the limitations of CO_2 mass transport.[31] Partial current densities for CO (j_{CO}) were observed in the range from 2.2 to 3.8 mA/cm^2 for the NW photoelectrodes in between −0.20 V to −0.37 V vs RHE (Figure 3b), exhibiting an average enhancement factor of 2.8 compared to the planar counterpart showing j_{CO} from 0.6 to 1.8 mA/cm^2 within the same potential range. In other words, when evaluated in terms

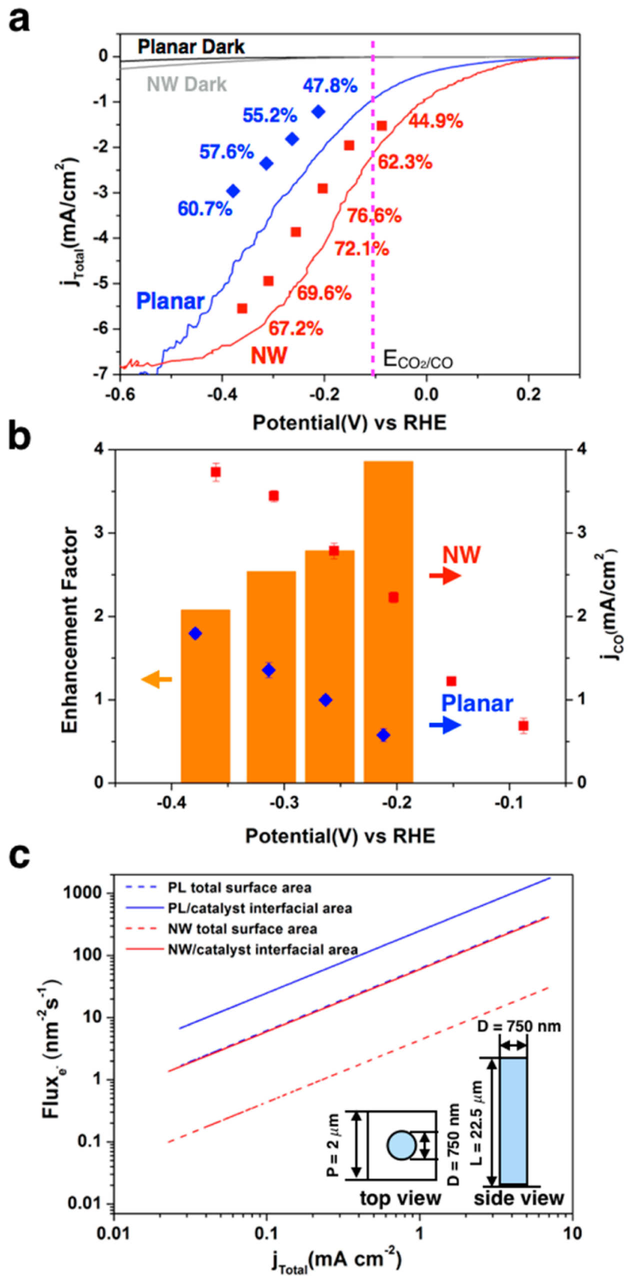

Figure 3. Photoelectrochemical reduction of CO_2 using integrated photoelectrodes. (a) Comparison between Au_3Cu NP assembled Si PL and NW photoelectrodes in catalytic activity and FE for CO_2 conversion to CO. Solid lines present linear sweep voltammetry (10 mV s^{-1}) of both substrates under dark and under illumination. Each point represents total current density from the geometric area of the photoelectrodes during chronoamperometry and the numbers indicate faradaic efficiency toward CO. (b) Partial current density for CO generation of Au_3Cu NP assembled substrates and enhancement of NW over PL for comparison. All the measurements were under 20 mW/cm^2 of 740 nm illumination (calibrated with standard Si photodiode) with photon flux above silicon band gap comparable to one-third of that obtained from 100 mW/cm^2, air mass 1.5 solar illumination to take into account CO_2 mass-transport limitations in 0.1 M $KHCO_3$ (pH = 6.8) at 1 atm CO_2 and room temperature. Error bars at each potential are based on multiple measurements. (c) Estimation of photogenerated electron fluxes (Flux$_{e^-}$) over the output current range on both substrates. Flux$_{e^-}$ considering substrate total surface area (dashed line) and substrate/catalyst interfacial area (solid line) are both calculated. The flux$_{e-}$ considering PL total surface area

Figure 3. continued

around the saturated photocurrent (~430 electrons/(nm^2·s)) matches well with the typical value of planar n$^+$p-Si (~1200 electrons/(nm^2·s) under one-sun illumination[32] and corrected by photon flux used in this work.). When considering the real interfacial area determined by NP assembly on both substrates, quantitative analysis of NP coverage (7.30% and 24.9% on NW and PL, respectively) is used. The inset shows NW substrate dimensions used for calculation.

of additional bias (overpotential) needed to drive CO_2-to-CO conversion, NW photoelectrodes required less overpotentials (~120 mV lower) compared to the planar photoelectrodes. The NW geometry allows decreasing the photogenerated electron flux (Flux$_{e^-}$) over its large surface area (Figure 3c), alleviating the turnover requirement of the loaded catalyst and consequently reducing the necessary overpotential.[32] Compared to the planar substrate, NW array with high roughness factor in this work allows Flux$_{e^-}$ dilution by 14.25 times, when considering its entire surface area, as presented by the dotted lines in Figure 3c.

This is, however, the idealized case, and to benefit the most from having a high surface area light-harvesting support when catalysts are spatially coupled, the interfaced catalysts have to be well-dispersed across the entire surface so that a large contact area is formed to distribute the electron flux, together with a large number of active sites exposed for catalytic turnover. When the real interfacial area determined by NP assembly on both photoelectrodes (with coverage values 7.30% and 24.9% on the NW and PL, respectively) is considered, it is also clear that NWs were favorable in this aspect by directing uniform assembly of nanoparticle catalysts from its one dimensionality, which resulted in a consistently reduced Flux$_{e^-}$ by a factor of 4 with catalytic sites exposed to the largest degree in comparison to that of the planar (solid lines in Figure 3c). To be specific, in the case of maximal photogenerated electron extraction, the NP assembled NW photoelectrode exhibited reduced Flux$_{e^-}$ of 414 electrons/(nm^2·s) compared to that of the PL substrate with 1753 electrons/(nm^2·s). In addition, the effect of reduced overpotentials from electron flux dilution is further enhanced when the reaction under interest is sluggish with slow turnover and the relative increase in turnover is less per added overpotential. This is indeed the case for CO_2 reduction that requires greater amount of overpotential for turnover increase, especially in the operational current region (Figure S11) for solar-to-fuel conversion to be practical. Therefore, NW photoelectrodes are clearly advantageous in reducing overpotential for CO_2 reduction compared to the well-known proton reduction, by allowing each catalyst to operate at a diluted electron flux. From the performance observed, we could see that the NW, as a light absorber, has allowed effective charge transport to the assembled NPs for CO_2 reduction without disturbing their inherent catalytic activity. More importantly, by utilizing the unique value of one-dimensionality present in the NW system that allowed uniform assembly, target products could be effectively gained with decrease of electrocatalysis losses in the form of kinetic overpotentials.[33]

The integrated system was tested for an extended period of 18 h (Figure 4a). As shown, with minimal change in current density, CO was maintained as a major product during continuous operation exhibiting long-term capability for photoelectrochemical CO_2 reduction.[6−8] Furthermore, we tried to see if a third component could be incorporated to

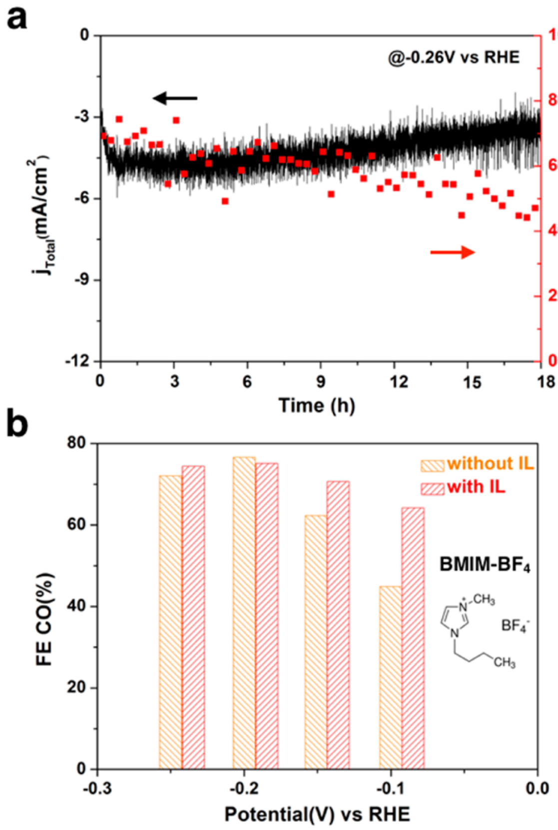

Figure 4. Photoelectrochemical performance in the long term and incorporating ionic liquid as a third component. (a) CO_2 reduction activity of Au_3Cu NP/Si NW photoelectrode for 18 h. Total current density and FE for CO at −0.26 V vs RHE. (b) Potential-dependent CO FEs of Au_3Cu NP/Si NW photoelectrode incorporating ionic liquid BMIM-BF_4. All the data were obtained in CO_2-saturated 0.1 M $KHCO_3$ under standard conditions (pH = 6.8).

enhance photoelectrochemical performance. Using the identical drop-casting approach, the addition of 1-butyl-3-methylimidazolium tetrafluoroborate (BMIM-BF_4)[21] can further enhance the CO selectivity in the low overpotential region, with FE rising from 44.9% to 64.2% at −0.09 V vs RHE (Figure 4b). The adsorption of BMIM-BF_4 on NP catalyst surface allows lowering the energy barriers for CO_2 reduction by complexation with the CO_2 reduction intermediate, thereby leading to favorable charge transport toward CO_2 reduction rather than competing hydrogen evolution. This further illustrates how combining multiple components using the simple method described here could be effective for artificial photosynthesis.

Beyond the already proven benefits of Si NWs as an attractive material for photoelectrochemical applications,[34,35] here, we have shown an additional advantage of the one-dimensional geometry allowing a simple and effective integration process for photoelectrochemical reduction of CO_2. The assembly process demonstrated shows that Si NWs have the potential to perform as a general platform for interfacing a wide range of CO_2 reducing NP catalysts for light-driven applications. As part of the process in constructing a sophisticated system of optimized components, this approach will facilitate the advances of artificial photosynthesis combining synthetic nanoparticle catalysts.

■ ASSOCIATED CONTENT

Ⓢ Supporting Information

The Supporting Information is available free of charge on the ACS Publications website at DOI: 10.1021/acs.nanolett.6b02321.

Detailed methods and characterization of nanoparticles assembled on nanowire arrays and their photoelectrochemical CO_2 reduction properties. (PDF)

■ AUTHOR INFORMATION

Corresponding Author

*E-mail: p_yang@berkeley.edu.

Author Contributions

(Q.K. and D.K.) These authors contributed equally to this work.

Author Contributions

Q.K., D.K., and P.Y. designed the experiments and wrote the paper. Q.K., C.L., and Y.S. fabricated silicon nanowire array devices. D.K. synthesized and characterized nanoparticles. Q.K., D.K., C.L., and Y.L. carried out the assembly process and performed photoelectrochemical measurements. Y.Y. carried out STEM imaging and elemental mapping. All authors discussed the results and commented on the manuscript.

Notes

The authors declare no competing financial interest.

■ ACKNOWLEDGMENTS

This work was supported by U.S. Department of Energy (contract no. DE-AC02-05CH11231, PChem). We thank the nanofabrication facilities in Marvell Nanofabrication Laboratory, imaging facilities at the Molecular Foundry, and the NMR facility, College of Chemistry, University of California, Berkeley. Work at the Molecular Foundry was supported by the Office of Science, Office of Basic Energy Sciences, of the U.S. Department of Energy under Contract No. DE-AC02-05CH11231. Q.K. acknowledges support from Suzhou Industrial Park Fellowship. D.K. acknowledges support from Samsung Scholarship.

■ REFERENCES

(1) White, J. L.; Baruch, M. F.; Pander, J. E., III; Hu, Y.; Fortmeyer, I. C.; Park, J. E.; Zhang, T.; Liao, K.; Gu, J.; Yan, Y.; Shaw, T. W.; Abelev, E.; Bocarsly, A. B. *Chem. Rev.* **2015**, *115*, 12888−12935.

(2) Kim, D.; Sakimoto, K. K.; Hong, D.; Yang, P. *Angew. Chem., Int. Ed.* **2015**, *54*, 3259−3266.

(3) Schreier, M.; Luo, J.; Gao, P.; Moehl, T.; Mayer, M. T.; Grätzel, M. *J. Am. Chem. Soc.* **2016**, *138*, 1938−1946.

(4) Liu, C.; Gallagher, J. J.; Sakimoto, K. K.; Nichols, E. M.; Chang, C. J.; Chang, M. C.; Yang, P. *Nano Lett.* **2015**, *15*, 3634−3639.

(5) Woolerton, T. W.; Sheard, S.; Reisner, E.; Pierce, E.; Ragsdale, S. W.; Armstrong, F. A. *J. Am. Chem. Soc.* **2010**, *132*, 2132−2133.

(6) Barton, E. E.; Rampulla, D. M.; Bocarsly, A. B. *J. Am. Chem. Soc.* **2008**, *130*, 6342−6344.

(7) Qiu, J.; Zeng, G.; Ha, M.; Ge, M.; Lin, Y.; Hettick, M.; Hou, B.; Alexandrova, A. N.; Javey, A.; Cronin, S. B. *Nano Lett.* **2015**, *15*, 6177−6181.

(8) Choi, S. K.; Kang, U.; Lee, S.; Ham, D. J.; Ji, S. M.; Park, H. *Adv. Energy Mater.* **2014**, *4*, 1301614.

(9) Liu, C.; Dasgupta, N. P.; Yang, P. *Chem. Mater.* **2014**, *26*, 415−422.

(10) Liu, C.; Tang, J.; Chen, H. M.; Liu, B.; Yang, P. *Nano Lett.* **2013**, *13*, 2989−2992.

(11) Mayer, M. T.; Du, C.; Wang, D. *J. Am. Chem. Soc.* **2012**, *134*, 12406−12409.

(12) Dai, P.; Xie, J.; Mayer, M. T.; Yang, X.; Zhan, J.; Wang, D. *Angew. Chem., Int. Ed.* **2013**, *52*, 11119−11123.

(13) Paracchino, A.; Laporte, V.; Sivula, K.; Grätzel, M.; Thimsen, E. *Nat. Mater.* **2011**, *10*, 456−461.

(14) Tilley, S.; Schreier, M.; Azevedo, J; Stefik, M.; Graetzel, M. *Adv. Funct. Mater.* **2014**, *24*, 303−311.

(15) Reece, S. Y.; Hamel, J. A.; Sung, K.; Jarvi, T. D.; Esswein, A. J.; Pijpers, J. J.; Nocera, D. G. *Science* **2011**, *334*, 645−648.

(16) Hou, Y.; Abrams, B. L.; Vesborg, P. C. K.; Björketun, M. E.; Herbst, K.; Bech, L.; Setti, A. M.; Damsgaard, C. D.; Pedersen, T.; Hansen, O.; Rossmeisl, J.; Dahl, S.; Nørskov, J. K.; Chorkendorff, I. *Nat. Mater.* **2011**, *10*, 434−438.

(17) AlOtaibi, B.; Fan, S.; Wang, D.; Ye, J.; Mi, Z. *ACS Catal.* **2015**, *5*, 5342−5348.

(18) Torralba-Peñalver, E.; Luo, Y.; Compain, J.-D.; Chardon-Noblat, S.; Fabre, B. *ACS Catal.* **2015**, *5*, 6138−6147.

(19) Gao, D.; Zhou, H.; Wang, J.; Miao, S.; Yang, F.; Wang, G.; Wang, J.; Bao, X. *J. Am. Chem. Soc.* **2015**, *137*, 4288−4291.

(20) Kim, D.; Resasco, J.; Yu, Y.; Asiri, A. M.; Yang, P. *Nat. Commun.* **2014**, *5*, 4948.

(21) Zhu, W.; Michalsky, R.; Metin, Ö.; Lv, H.; Guo, S.; Wright, C. J.; Sun, X.; Peterson, A. A.; Sun, S. *J. Am. Chem. Soc.* **2013**, *135*, 16833−16836.

(22) Schreier, M.; Curvat, L.; Giordano, F.; Steier, L.; Abate, A.; Zakeeruddin, S. M.; Luo, J.; Mayer, M. T.; Grätzel, M. *Nat. Commun.* **2015**, *6*, 7326.

(23) Delacourt, C.; Ridgway, P. L.; Kerr, J. B.; Newman, J. *J. Electrochem. Soc.* **2008**, *155*, B42−B49.

(24) Zhan, Z.; Kobsiriphat, W.; Wilson, R. J.; Pillai, M.; Kim, I.; Barnett, A. S. *Energy Fuels* **2009**, *23*, 3089−3096.

(25) Jiao, F.; Li, J.; Xiao, J.; Li, H.; Ma, H.; Wei, M.; Pan, Y.; Zhou, Z.; Li, M.; Miao, S.; Li, J.; Zhu, Y.; Xiao, D.; He, T.; Yang, J.; Qi, F.; Fu, Q.; Bao, X.; Pan, X. *Science* **2016**, *351*, 1065−1068.

(26) Yunker, P. J.; Still, T.; Lohr, M. A.; Yodh, A. G. *Nature* **2011**, *476*, 308−311.

(27) Chi, L. F.; Gleiche, M.; Fuchs, H. *Nature* **2000**, *403*, 173−175.

(28) Huang, J.; Kim, F.; Tao, A. R.; Connor, S.; Yang, P. *Nat. Mater.* **2005**, *4*, 896−900.

(29) Zheng, N.; Stucky, G. D. *J. Am. Chem. Soc.* **2006**, *128*, 14278−14280.

(30) Rabani, E.; Reichman, D. R.; Geissler, P. L.; Brus, L. E. *Nature* **2003**, *426*, 271−274.

(31) Kuhl, K. P.; Hatsukade, T.; Cave, E. R.; Abram, D. N.; Kibsgaard, J.; Jaramillo, T. F. *J. Am. Chem. Soc.* **2014**, *136*, 14107−14113.

(32) Su, Y.; Liu, C.; Brittman, S.; Tang, J.; Fu, A.; Kornienko, N.; Kong, Q.; Yang, P. *Nat. Nanotechnol.* **2016**, *11*, 609.

(33) Walter, M. G.; Warren, E. L.; McKone, J. R.; Boettcher, S. W.; Mi, Q.; Santori, E. A.; Lewis, N. S. *Chem. Rev.* **2010**, *110*, 6446−6473.

(34) Boettcher, S. W.; Spurgeon, J. M.; Putnam, M. C.; Warren, E. L.; Turner-Evans, D. B.; Kelzenberg, M. D.; Maiolo, J. R.; Atwater, H. A.; Lewis, N. S. *Science* **2010**, *327*, 185−187.

(35) Kelzenberg, M. D.; Boettcher, S. W.; Petykiewicz, J. A.; Turner-Evans, D. B.; Putnam, M. C.; Warren, E. L.; Spurgeon, J. M.; Briggs, R. M.; Lewis, N. S.; Atwater, H. A. *Nat. Mater.* **2010**, *9*, 239−244.